

Guy Nusholtz
Chrysler Corp.

Deguan Wang
Visiting Scholar

E. Benjamin Wylie
Department of Civil and
Environmental Engineering
University of Michigan
Ann Arbor, Michigan 48109-2125

Air Bag Momentum Force Including Aspiration

A gas-jet momentum force drives the air bag into position during a crash. The magnitude of this force can change as a result of aspiration. To determine the potential magnitude of the effect on the momentum force and mass flow rate in an aspirated system, a series of experiments and simulations of those experiments was conducted. The simulation consists of a two-dimensional unsteady isentropic CFD model with special "infinite boundaries." One of the difficulties in simulating the gas-jet behavior is determining the mass flow rate. To improve the reliability of the mass flow rate input to the simulation, a sampling procedure involving multiple tests was used, and an average of the tests was adopted. © 1995 John Wiley & Sons, Inc.

INTRODUCTION

To help protect both the driver and the front seat passenger in a frontal crash, the air bag has been developed as a supplemental restraint system. When a vehicle crash occurs, the air bag has to deploy fast enough to be in a position to manage the occupant's energy and prevent interaction with interior hard structures. The air-bag response and its effect on the occupant after deployment have been studied and modeled extensively; however, the deployment process has only recently received attention. One reason has been the computational effort necessary to model the gas dynamics of the unsteady compressible flow that occurs as the air bag fills.

A current area of research has been the gas jet that issues from the mouth of the air-bag canister

and pushes the air bag toward the occupant. This gas jet has been studied in a limited manner without a bag, that is, the gas jet forms in open air. Although this type of research simplifies the problem and allows for experimentally determined responses, it requires the use of extensive computation and accurately determined input values, such as mass flow rate and temperature.

Toward the final goal of understanding the deployment process, the air bag gas jet has been investigated using an isentropic, unsteady, two-dimensional, nonviscous compressible flow model. However, to use this model to study the gas jet in open air and compare it to experimental data requires the use of a large receiving domain. This results in large core storage and excessive computational time. A simple but effective boundary treatment, named the "infinite bound-

Received August 8, 1994; Accepted October 18, 1994.

Shock and Vibration, Vol. 2, No. 2, pp. 99-109 (1995)
© 1995 John Wiley & Sons, Inc.

CCC 1070-9622/95/020099-11

ary," has been developed, and can be used under appropriate conditions to represent the response from beyond the boundary. Therefore, the experimental results of an air bag gas jet issuing into open air can be modeled with a much smaller receiving domain, with major reductions in computer core storage and computing time. The goal of an infinite boundary, in this study, is to transmit wave energy from the air-bag generator source, while reflecting only that portion of the energy returned naturally by the distributed parameters of infinite space. There is unlikely to be a unique solution that will handle all of the possible conditions in air-bag deployment. Therefore, different implementations of the infinite boundaries are needed to represent the particular conditions being simulated. The range of applicability of each type must be understood for effective implementation.

In addition to numerical methods and their effect on simulation of results, there is the need to insure that the input data to the model represents the events that occurred in the experiment. Input data, such as mass flow rate coming from the inflator, are not easily determined from a single test. There is currently no way to determine mass flow rate during an experiment. Instead, a similar system is tested in a special "tank test," where mass flow rates may be determined. Then it is assumed that the mass flow rate in the air-bag experiment is the same as the mass flow rate in the tank test. However, there can be significant variance from tank test to tank test or experiment to experiment. A sampling procedure is utilized to provide a reasonable level of confidence in the results. With regard to mass flow rate, aspirated systems obtain some of the gas that fills the bag from open air and not the gas generator. This additional mass flow cannot be obtained from a tank test, and special considerations need to be made.

This study expands on previous work and presents new computational and experimental data on the air bag gas jet. The goal is to develop a better understanding of the air bag gas jet momentum force for both aspirated and non-aspirated systems, and to demonstrate the use of infinite boundaries in this calculation. Information on the potential effects of aspiration on mass flow, gas-jet formation, and momentum force is also presented. In addition a statistical "dual pressure" method is used to obtain a better mass flow estimate for a given set of experiments.

EXPERIMENTAL PROCEDURES

Momentum Force Measurement

An actual air-bag system consists of a housing (canister), an inflator (gas generator), and air-bag fabric. The drum test device (Fig. 1) used to measure the gas-jet momentum consisted of a cylindrical drum fitted with a triaxial accelerometer and an air-bag system (Nusholtz et al., 1991), without the bag fabric. The cylinder was connected to an "I" beam suspended from the ceiling by overhead cables. The canister was attached to a rigid supporting frame. In the aspirated and nonaspirated tests reported here, a passenger air-bag module was used. Although the nonaspirated canister allows flow to occur only out of the mouth of the system, the aspirated canister, riddled with holes that occupied over 70% of the surface, allowed flow through the back of the system. The air-bag fabric was removed to allow the gas jet to act directly on the drum. The force on the drum was obtained by multiplying its mass (50 kg) by its acceleration.

For each momentum force experiment, more than one drum test was run. There were three nonaspirated tests and five air-aspirated experiments. The momentum force time history shown later was obtained from the average of the drum tests.

Mass Flow Rate Measurement

The mass flow rate was obtained through the use of a large receiving tank (100 L) that contains the inflator. Measurements are the inflator pressure history, the tank pressure history, and final temperature. Conceptually it should be relatively direct to compute the time history of the inflator mass flow rate from the pressure and temperature sensor readings. Such is not the case due to

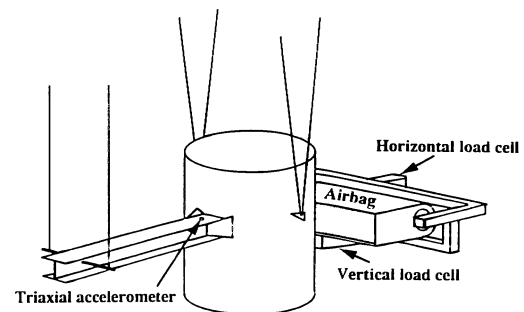


FIGURE 1 The experimental setup.

the hostile environment, and due to considerable variability between inflators. Robust temperature probes with sufficiently fast response times are not available to measure the temperature inside the inflator. Sensors to provide pressure histories for the inflator also are not always accurate for a number of reasons, one being that generate or particulate matter may block the pressure measurements. Inflators used in the tests may not be identical, and the inflators used in the tank tests could not be the ones used in the drum momentum force tests.

The procedure adopted to produce the mass flow history, needed for experimental evaluation and for numerical simulation, is first discussed, followed by detailed equations. A sampling (statistical) procedure was used in order to reduce variability and to provide consistent mass flow rate data. From a single lot of inflators, 15 were randomly chosen. Of the 15 inflators, 10 were used in the tank tests and five were set aside for the drum test. For the tank tests the inflator weight was measured before and after to provide a measure of the total mass issued into the tank, and during the test the inflator pressure history, the receiving tank pressure history, and the final temperature were recorded. If the maximum tank pressure varied between tests by more than 5%, then the lot was rejected. The inflator pressure history and the total mass are the most sensitive parameters. Because the inflator pressure measurement may contain inaccuracies that lead to large deviation from the true mass flow rate, a minimum of eight inflator pressure measurements without experimental contamination was required. Contamination was determined by making a comparison of the total mass obtained by integration of the inflator mass flow rate and the measured total mass. If the two differed by more than 5%, then that inflator's results were not used. If the above criteria were met, the five remaining modules were then used in the drum test. In the drum test, the pressure inside the inflator was measured and used to calculate the mass flow rate. If this measured pressure was outside the range of those that were obtained in the tank pretest, that drum test was rejected. Otherwise the average of the mass flow rate obtained from the tank test was used for the numerical model calculations. Although this procedure did not completely remove the experimental error, it helped to reduce test-to-test variation, and it addressed the problems of not being able to

measure the mass flow rate and temperature of the tested system.

Calculation of Mass Flow Rate of Inflator

By assuming critical flow (sonic flow) at the minimum open area of an orifice (throat), the mass flow rate is

$$\dot{m} = \rho^* A^* V^*, \quad (1)$$

where the asterisks indicate conditions in the throat at sonic flow, \dot{m} = mass flow rate, ρ = density of gas, A = the cross-sectional area, and V = the velocity. By assuming that the gas flow is isentropic (Streeter and Wylie, 1985), conditions in the throat can be related to conditions inside the inflator

$$\begin{aligned} \frac{T^*}{T_0} &= \frac{2}{\kappa + 1}; \quad \frac{p^*}{p_0} = \left(\frac{2}{\kappa + 1} \right)^{\kappa/(\kappa-1)}; \\ \frac{\rho^*}{\rho_0} &= \left(\frac{2}{\kappa + 1} \right)^{1/(\kappa-1)}, \end{aligned} \quad (2)$$

where T^* , p^* , and ρ^* are the temperature, pressure, and density at the throat, T_0 , p_0 , and ρ_0 are the temperature, pressure, and density inside the inflator, and κ = the specific heat ratio. Substitution of Eqs. (2) into Eq. (1) leads to

$$\dot{m} = \frac{A^* p_0}{\sqrt{T_0}} \sqrt{\frac{\kappa}{R} \left(\frac{2}{\kappa + 1} \right)^{(\kappa+1)/(\kappa-1)}}, \quad (3)$$

where R = gas constant. Because 99% of the gas from an inflator is nitrogen, then $\kappa = 1.4$ and $R = 297 \text{ m} \cdot \text{N}/\text{kg} \cdot \text{°K}$, and

$$\dot{m} = \frac{0.686 A^* p_0}{\sqrt{R} \sqrt{T_0}}. \quad (4)$$

For a sharp edged orifice, a discharge coefficient is needed that includes a contraction coefficient and a velocity coefficient. Although the inflator pressure history may be measured with some reliability, the temperature history cannot. The time history of temperature is estimated from fuel (used in the inflator) burning tests.

Two methods were used to check the consistency of the total mass of gas from each inflator: one used the final temperature and pressure from the tank test, and the second used the weight of

the inflator before and after discharge. In the first method the mass was calculated from the perfect gas law

$$m_f = \frac{p_f \mathcal{V}}{RT_f} \quad (5)$$

where T_f , p_f , and m_f indicate the final values of temperature, pressure, and total mass, and \mathcal{V} is the tank volume. If the difference between this calculated total mass m_f and the total mass from weighing the inflator before and after the test was less than 5%, then this m_f was used for verifying and correcting the calculated mass flow rate from Eq. (4). The mass flow rate calculated with Eq. (4) was adjusted proportionately so the total mass, obtained by integrating \dot{m} over time, equalled the value obtained with Eq. (5).

NUMERICAL MODEL

The detailed derivation of the numerical model and boundary treatment are presented in the studies of Wang and Wylie (1993) and Wylie (1984). Only the basic equations, the integrated compatibility equations, the infinite boundary, and the treatment of the aspiration hole boundary condition are described here. The computational domain for the numerical model in this application is shown in a later figure.

The two-dimensional unsteady compressible gas flow is governed by the following set of non-linear equations:

$$L_0 = u \frac{\partial p}{\partial x} + v \frac{\partial p}{\partial y} + \frac{\partial p}{\partial t} + \rho c^2 \frac{\partial u}{\partial x} + \rho c^2 \frac{\partial v}{\partial y} = 0 \quad (6)$$

$$L_1 = \frac{\partial p}{\partial x} + \rho u \frac{\partial u}{\partial x} + \rho v \frac{\partial u}{\partial y} + \rho \frac{\partial u}{\partial t} = 0 \quad (7)$$

$$L_2 = \frac{\partial p}{\partial y} + \rho u \frac{\partial v}{\partial x} + \rho v \frac{\partial v}{\partial y} + \rho \frac{\partial v}{\partial t} = 0 \quad (8)$$

$$L_3 = \frac{\partial u}{\partial y} + \frac{\partial v}{\partial x} - \left(\frac{\partial u}{\partial y} + \frac{\partial v}{\partial x} \right) = 0. \quad (9)$$

In these equations, p , u , and v are pressure and velocity components in x and y directions, respectively; t = time; ρ = the density of the fluid; and c = acoustic velocity. Equation (6) represents the conservation of mass condition including the sound speed definition $dp = c^2 d\rho$. Equations (7) and (8) are the momentum equations in

the x and y directions. Equation (9), which merely states an identity, completes the set of equations.

A combination of these four equations, using linear multipliers λ_1 , λ_2 , and λ_3 , is carried out in the following manner: $L_0 + \lambda_1 L_1 + \lambda_2 L_2 + \lambda_3 L_3 = 0$, which leads to a set of ordinary equations. By defining

$$q = \frac{1}{2} \left(\frac{\partial u}{\partial y} + \frac{\partial v}{\partial x} \right) \quad (10)$$

and taking into account the variation of density, ρ , through the isentropic relation

$$\frac{p}{\rho^\kappa} = C_a, \quad (11)$$

in which κ is the specific heat ratio, and C_a is a constant, the four primary variables become p , u , v , and q . The sets of equations ready for numerical integration become,

$$\frac{dx}{dt} = u + c \quad \frac{dy}{dt} = v + c \quad (12a)$$

$$C_{a1} p^{-[(\kappa+1)/2\kappa]} \frac{dp}{dt} + \frac{du}{dt} + \frac{dv}{dt} - 2qc = 0 \quad (12b)$$

$$\frac{dx}{dt} = u + c \quad \frac{dy}{dt} = v - c \quad (13a)$$

$$C_{a1} p^{-[(\kappa+1)/2\kappa]} \frac{dp}{dt} + \frac{du}{dt} - \frac{dv}{dt} + 2qc = 0 \quad (13b)$$

$$\frac{dx}{dt} = u - c \quad \frac{dy}{dt} = v - c \quad (14a)$$

$$C_{a1} p^{-[(\kappa+1)/2\kappa]} \frac{dp}{dt} - \frac{du}{dt} - \frac{dv}{dt} - 2qc = 0 \quad (14b)$$

$$\frac{dx}{dt} = u - c \quad \frac{dy}{dt} = v + c \quad (15a)$$

$$C_{a1} p^{-[(\kappa+1)/2\kappa]} \frac{dp}{dt} - \frac{du}{dt} + \frac{dv}{dt} + 2qc = 0 \quad (15b)$$

in which $C_{a1} = \sqrt{C_a^{1/\kappa}}$. Equations (12a) define the path of line $AP(C^{++})$ in x - y - t space shown in Fig. 2. Eq. (12b) is valid along this path. Each of the other equation pairs define specific lines in the x - y - t space, and a corresponding equation is

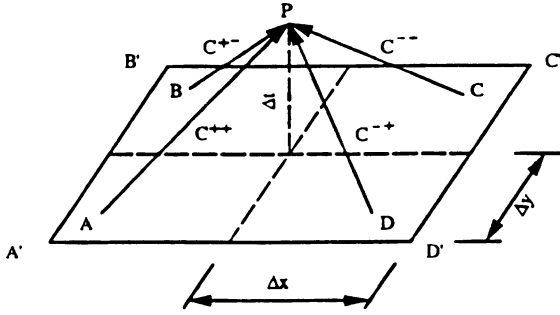


FIGURE 2 Path lines in x - y - t space.

valid along each line. At point P , Eqs. (12b)–(15b) are valid, providing the opportunity to solve for the four primary variables p , u , v , and q , assuming that they are known at the grid intersection points in the x - y plane, at the previous time step.

With a square computational grid $\Delta x = \Delta y$, and selected time step Δt , which varies during computation, integrating Eqs. (12b)–(15b) along the paths defined by Eqs. (12a)–(15a) leads to the following set of equations

$$C_{a2} p_P^{(\kappa-1)/2\kappa} + u_P + v_P - q_P c \Delta t = e_1 \quad (16)$$

$$C_{a2} p_P^{(\kappa-1)/2\kappa} + u_P - v_P + q_P c \Delta t = e_2 \quad (17)$$

$$C_{a2} p_P^{(\kappa-1)/2\kappa} - u_P - v_P - q_P c \Delta t = e_3 \quad (18)$$

$$C_{a2} p_P^{(\kappa-1)/2\kappa} - u_P + v_P + q_P c \Delta t = e_4 \quad (19)$$

in which $C_{a2} = C_{a1} 2\kappa / (\kappa - 1)$. The wave speed in the last term is assumed constant during the integration. An average local pressure from the previous time step, at points A' , B' , C' , and D' , is used in calculating the wave speed c . The terms on the right side, e_1 – e_4 , are evaluated based on the known transient conditions at the previous time step. The variables p_P , u_P , v_P , and q_P can be solved explicitly from Eqs. (16)–(19).

A boundary point may be treated with two equations from Eqs. (16) to (19), together with either two specified variables, one specified variable and one boundary equation, or two boundary equations that relate the free variables (Wang and Wylie, 1993; Wylie and Streeter, 1993). The aspiration hole, unique to this study, is described here, and is of the type with one additional boundary equation introduced, and one variable q approximated with the mean of the values at two adjacent interior nodes. The aspiration hole is considered as an orifice located at boundary nodes in the numerical model. The flow rate

through the hole is assumed proportional to the square root of the pressure drop across the hole. For the present purpose, it is supposed that the inflow begins when the pressure just inside the hole is below atmospheric pressure, and the inflow stops when the pressure just inside the hole is equal to or above atmospheric pressure. The flow rate through the orifice is calculated with the formula,

$$Q = C_d A_h \sqrt{2\Delta p / \rho_0} \quad (20)$$

in which C_d = velocity coefficient; A_h = cross-sectional area of the hole; $\Delta p = p_0 - p_h$, the pressure drop across the orifice; p_0 = the atmospheric pressure; p_h = the pressure just inside the hole; and ρ_0 = density of air at atmospheric pressure. To combine Eq. (15) with the integrated compatibility equations, the Q in Eq. (20) must be transformed into the velocity at the node u_P or v_P . For example,

$$u_P = C_d \frac{A_h}{2\Delta y \Delta z} \left(\frac{C_a}{p_0} \right)^{1/2\kappa} \sqrt{2(p_0 - p_P)} \quad (21)$$

in which Δz is a unit length. As an example, the hole at the left wall of the canister is considered (Fig. 3). Two integrated compatibility equations along the C^{-} , C^{+} lines should be used in this case.

$$C_{a2} p_P^{(\kappa-1)/2\kappa} - u_P - v_P - q_P c \Delta t = e_3 \quad (22)$$

$$C_{a2} p_P^{(\kappa-1)/2\kappa} - u_P + v_P + q_P c \Delta t = e_4. \quad (23)$$

The combination of Eqs. (21), (22), and (23) yields a set of equations for computations at

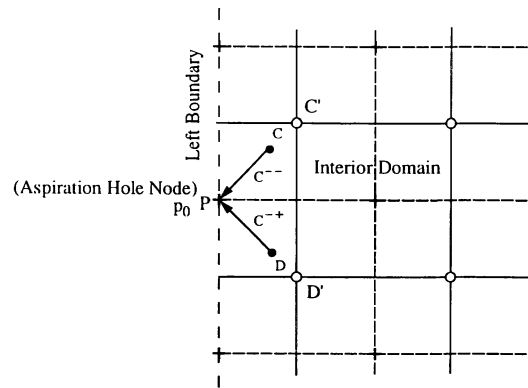


FIGURE 3 The aspiration hole treatment at left boundary.

nodes representing holes at the left wall of canister.

$$q_P = \frac{1}{2} (q_{C'} + q_{D'}) \tag{24}$$

$$v_P = \frac{1}{2} (e_4 - e_3) - q_P C \Delta t \tag{25}$$

$$C_{a2} p_P^{(\kappa-1)/2\kappa} - C_d \frac{A_h}{2\Delta y} \left(\frac{C_a}{p_0} \right)^{1/2\kappa} \tag{26}$$

$$\sqrt{2(p_0 - p_P)} - \frac{1}{2} (e_3 + e_4) = 0$$

$$u_P = C_d \frac{A_h}{2\Delta y} \left(\frac{C_a}{p_0} \right)^{1/2\kappa} \sqrt{2(p_0 - p_P)}. \tag{27}$$

The pressure p_P is solved from Eq. (26) by the bisection method. A similar set of equations can be derived for the aspiration holes at the other walls of the canister.

Infinite Boundary

An infinite boundary used in calculations of the air-bag system discharging into open air, should ideally provide the same response to a transient as an infinitely large domain. Such a boundary is possible for low-Mach-number-linearized-unsteady one-dimensional flow (Wylie and Streeter, 1993). However, nonlinear multidimensional unsteady flows present problems that are not always easily addressed. The nonlinearity, which is likely to cause partial reflection of the wave energy back to the source, may be the result of viscosity, frequency-dependent material properties, large variations in Mach number, etc. However, all partial reflections are not inaccuracies; the infinite boundary condition must account for reflections generated by the nonlinear distributed properties of infinite space, and for attenuation due to geometric properties of the multidimensional field. Therefore, any infinite boundary is likely to be an approximation at best. There is unlikely to be a unique solution to handle all of the possible conditions that occur in air-bag gas-jet simulation. Two types of infinite boundaries are used in the simulation of the drum test. One is called interpolation and projection (type A), and the second is called extended exterior characteristic-like line (type B). Numerical computations show that the type A infinite boundary is useful when the velocity gradient

along the boundary is high, but it has the disadvantage of a tendency for the pressure to drift somewhat from reference steady state in an unbounded area. Type B does not have the drift problem, but is mostly applicable to the open boundary where the velocity gradient is relatively small.

Interpolation and Projection. In unsteady flow, like the gas jet from an air bag, the properties of a disturbance (pressure, velocity) can be considered coming from the position where the disturbance was situated at an earlier time. The propagation of the disturbance is mathematically represented through the use of characteristic lines; a characteristic line in mathematical space represents, conceptually, a locus in a physical system along which disturbances travel without losing their properties. It is therefore possible to set up two virtual nodes (P' , P'') outside the boundary. They are one Δx away from the actual boundary of the computational domain and at time level n . Information is projected along characteristic-like lines to the virtual nodes (Fig. 4). The procedure requires interpolations in the spatial domain at two time steps earlier. Once the two virtual nodes are established then the boundary nodes behave as if they were interior nodes:

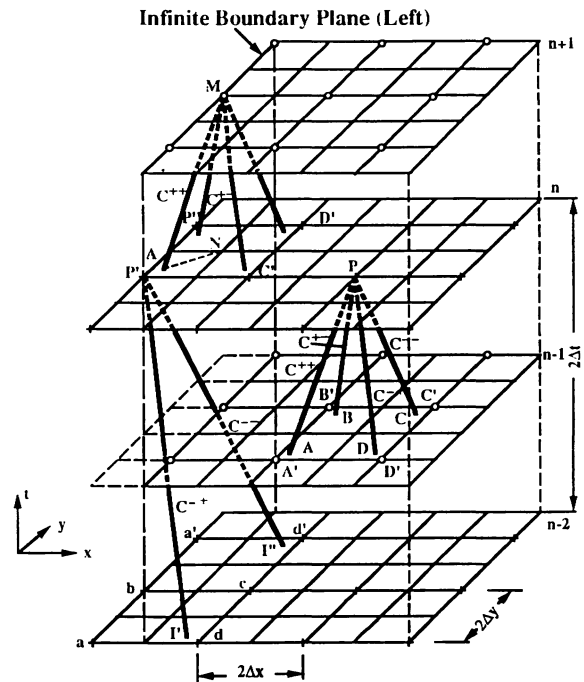


FIGURE 4 Characteristic projection (A) at infinite left boundary.

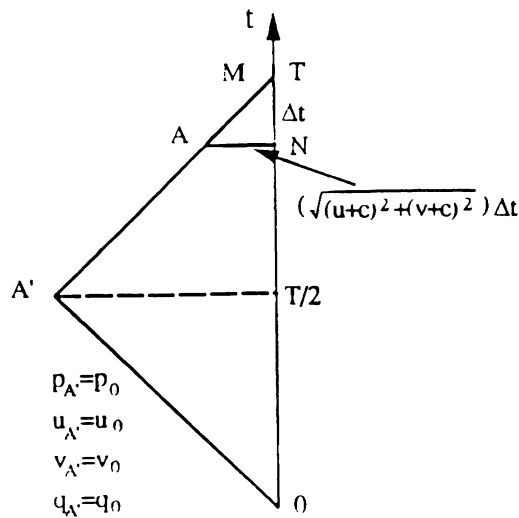


FIGURE 5 Extended exterior characteristic-like line (B) at infinite left boundary.

disturbances can pass through them and information, momentum and mass, can pass into and out of the receiving domain.

Computational results (Nusholtz et al., 1993) show that this infinite boundary procedure is most effective when the gas flow is significant and normal to the boundary. The gas jet in the experiment issues out of the air-bag canister and strikes the drum. The reflection of this gas jet generates a flow with a significant component normal to the boundary A-1 in Fig. 6. Therefore type A infinite boundary is chosen there.

Extended Exterior Characteristic-Like Line. To visualize this treatment it is necessary to refer to the ordinary differential equations, Eqs. (6)–(9), prior to integration to place them in finite difference form. The concept is one of extending the characteristics-like lines that exist outside the computational domain (i.e., those beyond the infinite boundary), back in time to the initial undisturbed conditions. The characteristics-like lines inside the domain are treated in the standard manner.

As an example, for the left infinite boundary plane shown in Fig. 5, the C^{++} and C^{+-} characteristics-like lines initiating at point M , would not terminate in the xy plane at time n , but would extend back in time as far as necessary to reach undisturbed conditions in infinite space. To illustrate, Fig. 5 shows a view in the plane of the C^{++} characteristics-like line (MNA , Fig. 4). Line $A'M$ is defined by Eq. (12a) along which Eq. (12b) is

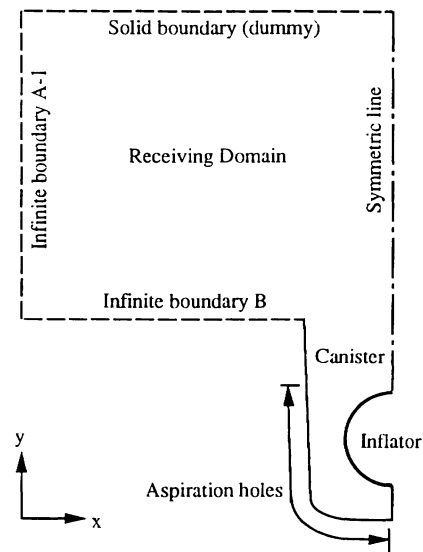


FIGURE 6 The schematized computational domain.

valid. Equation (12b) is integrated from point A' to M , rather than A to M . The first three terms are integrated exactly, regardless of the length of the line. The final term containing q requires an approximation in the integration. For irrotational flow, Eq. (10) becomes $q = du/dy = dv/dx$. If the value of q is not large, and if it is not changing rapidly along the infinite boundary, the following integration of Eq. (12b) is recommended:

$$C_{a2}(p_M^{(\kappa-1)/2\kappa} - p_{A'}^{(\kappa-1)/2\kappa}) + u_M - u_{A'} + v_M - v_{A'} - 2c(q_{A'} + q_M)/2(t_M - t_{A'}) = 0. \quad (28)$$

In the last term, $q_{A'} = 0$, because A' is always located in initial conditions, $t_M = T$, and $t_{A'} = T/2$. Thus, the last term becomes $cq_P T/2$, in which T is the total computational time, beginning at the initiation of the transient. The trapezoidal rule has been used. It is recognized that this approximation is poor if q varies dramatically, or if q is large, at the infinite boundary during the transient. The same type of integration is used along the C^{+-} characteristics-like line for the left infinite boundary. The other two lines, which extended into the computational domain, are treated like any other lines in the domain, and the compatibility equations are integrated over the current time step Δt . This means that Eqs. (14) and (15) must be modified, as well as Eqs. (18)–(21). The boundary next to the canister open face (labeled type B, Fig. 6) is reasonably passive with respect to the main flow pattern. This is the

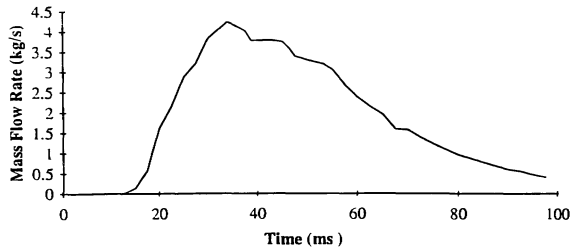


FIGURE 7 The input mass flow rate for aspirated system.

location where this second infinite boundary treatment is implemented.

SIMULATION OF EXPERIMENTAL RESULTS

The primary experimental result is the force exerted on the drum by the air bag gas jet. The goal of the computational procedure is to use the mass flow rate data as input to the model and predict the observed force on the drum. The measured momentum force time history is shown later for an aspirated air-bag system in Fig. 8, and for a nonaspirated system in Fig. 11. The momentum force in the numerical simulation is calculated using the pressure along the boundary that represents the cylindrical drum (Fig. 6) because the velocity v along that boundary is equal to zero.

$$\Delta F = p\Delta A \tag{29}$$

in which p represents the instantaneous pressure value along that boundary. The total reaction force is found by integrating over the entire area A of that boundary. In both cases the input mass flow rate for the simulation is computed directly from the measured time history of pressure inside the inflator, under the assumption that the flow at the exit of the hole of the inflator is sonic.

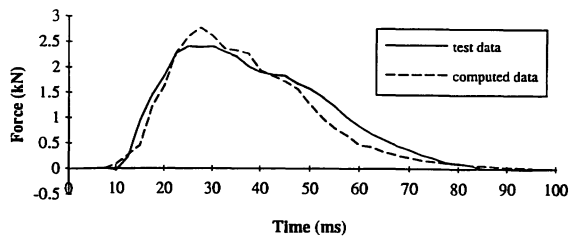


FIGURE 8 Comparison of computed and measured force on drum for aspirated system.

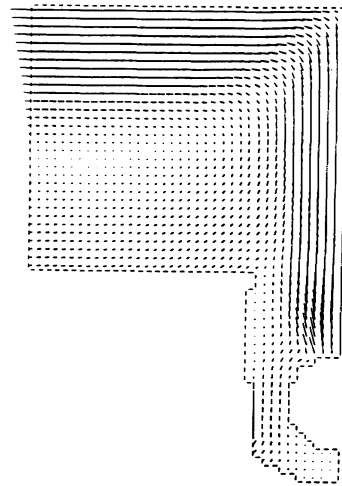


FIGURE 9 Comparison of computed and measured force on drum for aspirated system.

Aspirated System

The first example includes air aspiration. The issuing jet shoots directly toward the canister opening from the inflator. The boundary of the computational receiving domain consists of three types (Fig. 6). The line of symmetry is a solid boundary. The far part, parallel to the canister open face that represents the cylindrical drum, is a solid boundary. The part parallel to the symmetry line is type A infinite boundary because the velocity variations along this boundary are relatively large. The part next to the canister open face is type B infinite boundary as the velocity variations along that part are relatively small. The input mass flow rate is shown in Fig. 7. The time duration of transient to be analyzed is 0.100 s. Assumed initial pressure in the domain is $p_0 = 101.3$ kPa, assumed initial density is $\rho_0 = 1.2214$ kg/m³. Grid size $\Delta x = \Delta y = 0.2539$ cm.

The average aspiration rate, which is defined as the ratio of total aspirated mass to the total

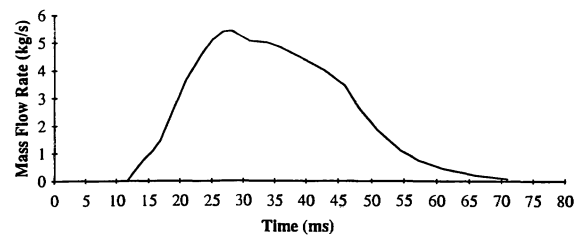


FIGURE 10 The input mass flow rate for nonaspirated system.

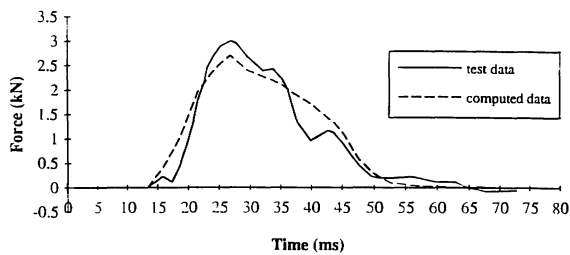


FIGURE 11 The flow pattern at an instant during the inflator discharge for aspirated system.

input mass, is about 20%. Figure 8 shows the comparisons of the computed and measured time histories of the force on the drum. The solid lines indicate the test data, and the dashed lines indicate the computed data. Figure 9 shows the flow pattern at an instant during the inflator discharge.

Figure 8 shows the force histories to be in reasonable agreement both in magnitude and pattern, although the computed force time history curve is narrower than the measured curve. Due to slightly different assumptions built into the computer model than actually exists in the physical model, the aspiration rate from computations is not likely to perfectly reflect the real aspiration process. The fact that the total impulse in the force record exceeds the computational impulse is further evidence that the aspiration rate may be somewhat differently distributed over the time period.

Nonaspirated System

The second example has no aspiration. The input mass flow rate is shown in Fig. 10. The issuing jet shoots transversely toward the canister wall from the inflator. The setup of the computational receiving domain is the same as in the aspirated system. The time duration of transient to be analyzed is 0.060 s. Assumed initial pressure in the domain is $p_0 = 101.3$ kPa, and assumed initial density is $\rho_0 = 1.2214$ kg/m³. Grid size $\Delta x = \Delta y = 0.2539$ cm. Figure 11 shows the comparisons of the computed and measured time histories of the force on the drum. The solid lines indicate the test data and the dashed lines indicate the computed data. Figure 12 shows the flow pattern at an instant during the inflator discharge.

Again the comparisons of the measured and computed time history of forces on the drum show good agreement, both in magnitude and pattern, in general. In this case, the measured

force is less uniform than what is calculated. With the inflator jet first striking the canister before being directed to the drum, the actual deformation of the canister, which is known to be significant, influences the velocity pattern. In the simulation model the canister is assumed rigid so this influence is not included. On the other hand, the total impulse is approximately the same in the two records. It may be noted that the computed dynamic force qualitatively follows the shape of the time variable inflator mass flow rate. In as much as the force is dominated by the momentum flux, it is natural that the force follows the pattern of the inflator mass flow.

DISCUSSION

Aspiration, as presented in the first example, may have several beneficial effects, such as a reduction in fuel, a reduction in air-bag gas temperature, and an increase in the magnitude of the momentum force. As an example of the latter potential benefit, the instantaneous peak force in example 1, at the point of maximum force, is 8.5% greater when computed with aspiration as compared with computations not including air aspiration. The total mass flux increase for the same inflator mass discharge is 20.0%.

To visualize the effect of aspiration on momentum force, the following discussion is presented. The momentum force at a section in a gas jet is given by

$$M = \dot{m}V \quad (30)$$

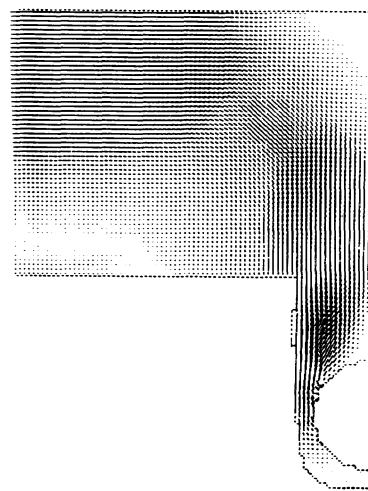


FIGURE 12 The flow pattern at an instant during the inflator discharge for nonaspirated system.

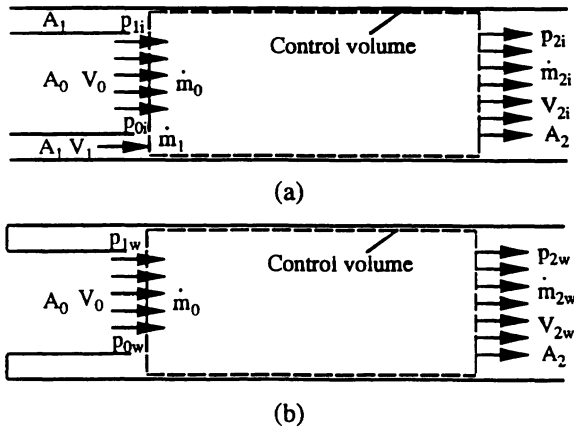


FIGURE 13 Control volume: (a) including aspiration and (b) without aspiration.

in which M = momentum flux, \dot{m} = mass flow rate, and V = the average velocity. The additional momentum force resulting from air aspiration may be estimated in the following manner. In Fig. 13, a high velocity gas jet with a mass flow rate of \dot{m}_0 is introduced through area A_0 and entrains a mass flow rate of \dot{m}_1 through an area of A_1 . It is assumed that the gases are completely mixed by the time they reach section 2, where the mass flow rate will be $\dot{m}_2 = \dot{m}_0 + \dot{m}_1$.

The linear momentum equation applied to control volume in Fig. 13 yields

$$p_0 A_0 + p_1 A_1 - p_2 A_2 = \dot{m}_2 V_2 - \dot{m}_1 V_1 - \dot{m}_0 V_0, \quad (31)$$

in which p_0 , p_1 , and p_2 are the average pressures, associated with the average densities of the fluid passing through areas A_0 , A_1 , and A_2 , respectively. The total force with aspiration included, F_i , is given by

$$\begin{aligned} F_i &= p_{2i} A_2 + \dot{m}_{2i} V_{2i} \\ &= p_{0i} A_0 + p_{1i} A_1 + \dot{m}_1 V_1 + \dot{m}_0 V_0. \end{aligned} \quad (32)$$

If the aspiration is removed ($\dot{m}_1 = 0$), then the linear momentum equation may be used to define the total force without aspiration, F_w :

$$\begin{aligned} F_w &= p_{2w} A_{2w} + \dot{m}_{2w} V_{2w} \\ &= p_{0w} A_0 + p_{1w} A_1 + \dot{m}_0 V_0. \end{aligned} \quad (33)$$

The force amplification factor due to aspiration may be written as

$$\frac{F_i}{F_w} = \frac{p_{0i} A_0 + p_{1i} A_1 + \dot{m}_1 V_1 + \dot{m}_0 V_0}{p_{0w} A_0 + p_{1w} A_1 + \dot{m}_0 V_0}. \quad (34)$$

Air density variation with pressure renders this equation difficult to evaluate numerically. As a limiting case a constant density example is assumed, i.e., $p_{0i} = p_{1i} = p_{0w} = p_{1w} = p_0$. Additionally this reference pressure is assumed to be local ambient conditions, i.e., $p_0 = 0$. With this assumption,

$$\frac{F_i}{F_w} = 1 + \frac{\dot{m}_1 V_1}{\dot{m}_0 V_0} = 1 + \frac{M_1}{M_0}$$

or

$$\frac{F_i}{F_w} = 1 + \left(\frac{\dot{m}_1}{\dot{m}_0} \right)^2 \frac{\rho_0 A_0}{\rho_1 A_1}. \quad (35)$$

As an example, if the area ratio $A_0/A_1 = 2$, and $\dot{m}_1/\dot{m}_0 = 0.2$, with $\rho_0 = \rho_1$, $F_i/F_w = 1.08$. This represents an 8% increase in force due to fluid aspiration. With modest pressure changes and the corresponding density changes, in an actual air aspirating apparatus, the force ratio is likely to be slightly different.

CONCLUSIONS

The numerical model presented herein provides computed output in reasonable agreement with measured data for two cases, one with air aspiration and one without. This agreement supports the position that the numerical model may be of considerable value in analysis and design of the dynamic behavior of inflator-canister air-bag systems.

Infinite boundaries have been shown to be an effective method of reducing the computational domain; however care must be exercised to be sure the particular implementation produces a realistic behavior.

Inasmuch as accurate inflator mass flow rate is essential for momentum calculation, an experimental sampling procedure is utilized to assure a reasonable level of confidence in the mass flow rate time history from the inflator. In addition, aspiration may increase the mass to the air bag. In this study this is demonstrated both experimentally and numerically to be about 20%. Additionally, there is a potential momentum force increase by aspiration. In the example herein, the increase is about 8%.

It is recognized that the simulations, both experimental and computational, are run without the actual air bag on the canister. The additional back pressure that would exist during early time of the deployment if the air bag were present would have some influence on the volume of air aspirated, and on the magnitude of the early time momentum force.

REFERENCES

- Nusholtz, G., Fong, W., and Wu, J., 1991, "Air Bag Wind Blast Phenomena Evaluation," *Experimental Techniques*, Vol. Nov.–Dec.
- Nusholtz, G., Wang, D. G., and Wylie, E. B., 1993, "Simulation Model of Air-bag Deployment Gas Flow," *ASME Annual Winter Meeting*, AMD-Vol. 169/BED-Vol. 25, New Orleans, November 1993, pp. 243–253.
- Streeter, V. L., and Wylie, E. B., 1985, *Fluid Mechanics*, 8th ed., McGraw–Hill, New York, pp. 287–290.
- Wang, D. G., and Wylie, E. B., 1993, "Two-Dimensional Unsteady Compressible Flow Model," *ASME Forum on Unsteady Flows*, FED-Vol. 157, Washington, DC, June 1993, pp. 119–127.
- Wylie, E. B., "Linearized Two-Dimensional Transients," 1984, *Journal of Fluids Engineering*, ASME, Vol. 106, pp. 227–232.
- Wylie, E. B., and Streeter, V. L., 1993, *Fluid Transients in Systems*, Prentice Hall, NJ, pp. 120–122.



Hindawi

Submit your manuscripts at
<http://www.hindawi.com>

